ACS OMEGA

Open Access

http://pubs.acs.org/journal/acsodf

Article

Piezoelectric, Thermoelectric, and Photocatalytic Water Splitting Properties of Janus Arsenic Chalcohalide Monolayers

Poonam Chauhan and Ashok Kumar*

Cite This: *ACS Omega* 2024, 9, 33723−33734

Read Online

ACCESS | Metrics & More | Article Recommendations | Supporting Information

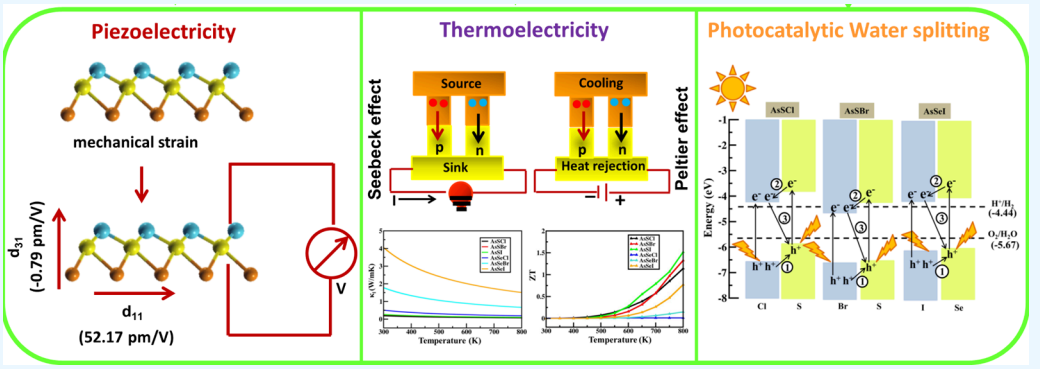

ABSTRACT: In this study, we systematically investigate the piezoelectric, thermoelectric, and photocatalytic properties of novel two-dimensional Janus arsenic chalcohalide monolayers, AsXX' (X = S and Se and X' = Cl, Br, and I) using density functional theory. The positive phonon spectra and ab initio molecular dynamics simulation plots indicate these monolayers to be dynamically and thermally stable. The mechanical stability of these monolayers is confirmed by a nonzero elastic constant (C_{ij}), Young's modulus (Y_{2D}), and Poisson ratio (ν). These monolayers exhibit strong out-of-plane piezoelectric coefficients, making them candidate materials for piezoelectric devices. Our calculated results indicate that these monolayers have a low lattice thermal conductivity (κ_l) and high thermoelectric figure of merit (zT) up to 1.51 at 800 K. These monolayers have an indirect bandgap, high carrier mobility, and strong visible light absorption spectra. Furthermore, the AsSCl, AsSBr, and AsSeI monolayers exhibit appropriate band alignment for water splitting. The calculated value of the corrected solar-to-hydrogen conversion efficiency can reach up to 19%. The nonadiabatic molecular dynamics simulations reveal the prolonged electron−hole recombination rates of 1.52 0.98, and 0.67 ns for AsSCl, AsSBr, and AsSeI monolayers, respectively. Our findings demonstrate these monolayers to be potential candidates in energy-harvesting fields.

1. INTRODUCTION

Energy-harvesting applications such as thermoelectricity,[1] piezoelectricity,[2,3] and photocatalytic water splitting[4] are highly efficient means to overcome the energy crises and environmental pollution problems. In thermoelectric phenomena, unexploited heat released in the environment from primary sources of energy can be utilize to produce environmentally friendly sustainable energy using various mechanisms such as the Seebeck effect and the Peltier effect.[5] The performance of these thermoelectric mechanisms is characterized in terms of dimensionless quantity zT ($zT = \frac{S^2\sigma}{\kappa}T$). The high value of the power factor, i.e., $S^2\sigma$, and low value of thermal conductivity (κ) give rise to a high value of thermoelectric performance. Further, in the case of piezoelectricity, mechanical energy can be converted into electrical energy by applying mechanical strain on the systems.[3,6] Also, the piezoelectric devices are beneficial to detect heart, brain, and other organ-related diseases.[7]

Solar energy-harvesting mechanisms such as photocatalytic water splitting[8] is the most economical methods to overcome the energy crisis and environmental pollution problem. The photocatalytic water splitting is the most stupendous method for the production of pollution-free green energy by availing of solar energy.[9] For commercial production of hydrogen, the solar-to-hydrogen conversion efficiencies (η_{STH}) should exceed 10%.[10]

For the implementation of these applications, researchers have investigated various types of materials. After the successful fabrication of graphene, a boom came in the field

Received: March 25, 2024
Revised: July 3, 2024
Accepted: July 5, 2024
Published: July 26, 2024

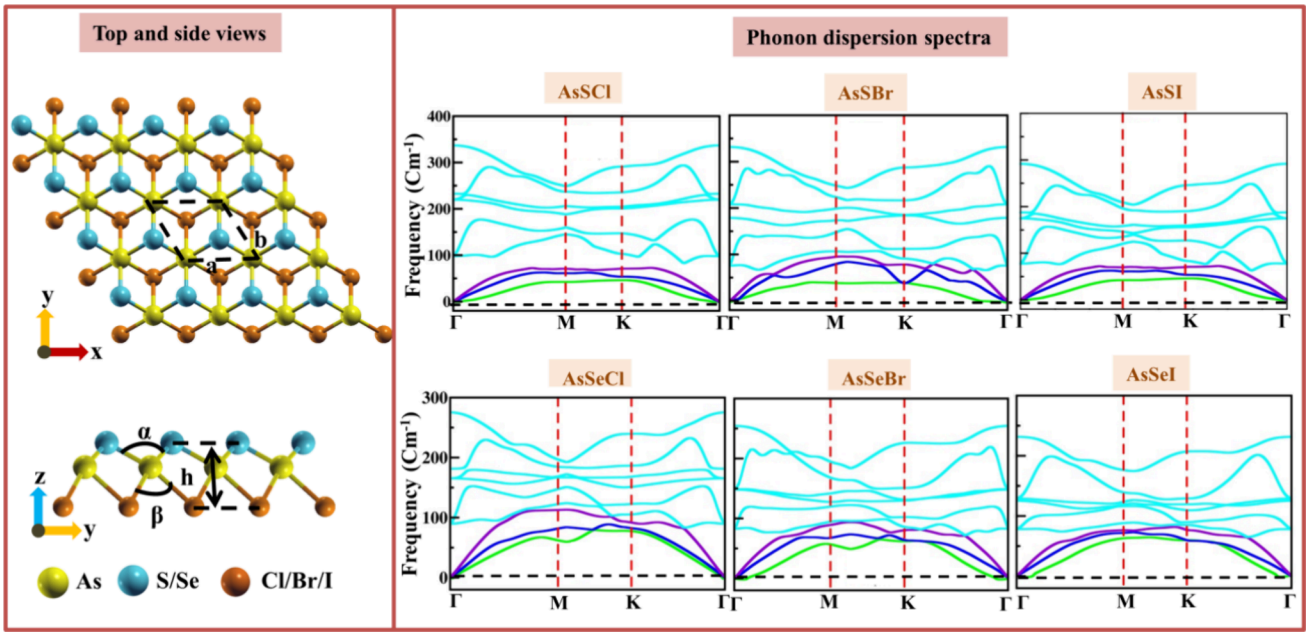

Figure 1. Top view, side view, and phonon dispersion spectra of Janus AsXX' monolayers. The green, blue, purple, and cyan phonon lines correspond to ZA, TA, LA, and optical modes, respectively.

of 2D materials.[11] Following the experimental synthesis of graphene, various 2D monolayers were fabricated experimentally, such as germanene,[12] silicene,[13] antimonene,[14] and bismuthene.[15] Apart from these, a new class of 2D materials, i.e., Janus monolayers, attracted researchers due to their distinct properties on different surfaces. The first experimentally fabricated Janus material is the Janus graphene monolayer, which is synthesized via surface functionalization methods, thus leading to the opening of bandgap in graphene.[16] After that, Janus MoSSe and Janus WSSe were synthesized experimentally.[17] Recently, Janus BiTeX (X = Cl, Br, and I) was synthesized experimentally via CVD and liquid-phase exfoliation methods.[18]

These experimental syntheses motivate researchers to further investigate analogous monolayers theoretically and experimentally. At 300 K, the zT values of Janus WSX (X = Se and Te),[19] PdSX (X = Se and Te),[20] AsTeX (X = Cl, Br, and I),[21] AsSBr,[22] $ZnMN_2$ (M = Ge, Sn, and Si; N = S, Se, and Te),[23] XClO (X = Cl and Ir),[24] NSiX (X = O, S, and Se),[25] and BiTeX (Cl and Br)[26,27] lie in the range of 0.0004−0.75. Out-of-plane asymmetry in Janus structures gives rise to an additional degree of freedom, which is utilized to tune the piezoelectric properties of Janus monolayers. The piezoelectric properties of 2D monolayers are specified by in-plane (d_{11}) and out-of-plane (d_{31}) piezoelectric coefficients. Janus TiXY (XY = SCl and SeBr),[28] group IV(A) Janus dichalcogenides,[29] YBrI,[30] $MoAZ_3H$ (A = Si and Ge: Z = N, P, and As),[31] BiXY (X = S, Se, and Te; Y = F, Cl, Br, and I),[32] PtXO (X = S and Se),[33] $MoSSiX_2$ (X = N, P, and As),[34] BMX_2 (M = Ga and In; X = S and Se),[35] M_2AB (M = Si, Ge, and Sn; A/B = N, P, and As),[36] and γ-Ge_2XX' (X, X' = S, Se, and Te)[37] show a very high out-of-plane piezoelectric behavior, which is beneficial for piezoelectric devices. Furthermore, the corrected solar-to-hydrogen conversion efficiencies of Janus monolayer-based photocatalysts such as WSSe,[38] MoSSe,[39] PtSSe,[40] WSeTe,[41] AsTeX (X= Cl and Br),[21] AsXY (X= Se and Te; Y = Br and I),[42] and AlXY (X= S and Se; Y= Cl, Br, and I)[43] exceed the 10% criteria for commercial use of photocatalysts.

Stimulated by experimental synthesis of the Janus monolayers,[18] we investigate the arsenic-based chalcohalide Janus monolayers, i.e., AsXX' (X = S and Se and X = Cl, Br, and I). The positive phonon dispersion spectra, *ab initio* molecular dynamics (AIMD) simulations, and elastic tensor coefficients quantified their dynamical, thermal, and mechanical stability, respectively. We explore these monolayers in various energy-harvesting fields such as piezoelectricity, thermoelectric, and photocatalytic water splitting. Further, these monolayers possess a very high carrier mobility and strong visible region optical absorption spectra. Last, we computed electron−hole recombination rates (τ) of Janus monolayers in the context of photocatalytic water splitting. Our computed results indicate that these monolayers have capabilities for various energy-harvesting applications.

2. COMPUTATIONAL DETAILS

We employed density functional theory within the Vienna ab initio simulation package (VASP)[44] to perform first-principles calculations. To include the link between electrons and ions, we used projected augmented-wave (PAW)[45] potentials, while generalized gradient approximation (GGA) parametrized by Perdew−Burke−Ernzerhof (PBE)[46] has been implemented to calculate exchange−correlation functionals. To confirm the well-founded calculation of electronic properties, the screened hybrid method HSE06 has been implemented.[47] We relax the structure until the Hellmann−Feynman forces decrease below 0.01 eV/Å. The energy convergence criteria between sequential steps for structural relaxation are fixed at 10^{-5} eV. For the sampling of the Brillouin zone, the Γ-centered k-mesh of 16 × 16 × 1[48] has been implemented. A vacuum of 17 Å is used to exterminate the interaction between the adjoining layers in a nonperiodic direction.

The phonon dispersion spectra calculations were performed using the DFPT method with a q-mesh of 8 × 8 × 1 and convergence threshold of 10^{-16} Ry as incorporated with the Quantum Espresso package.[49] The thermal stability of 2D AsXX' Janus monolayers has been validated by AIMD

https://doi.org/10.1021/acsomega.4c02874
ACS Omega 2024, 9, 33723−33734

Table 1. Elastic Coefficients (C_{11}, C_{12}, C_{13}, C_{44}, C_{33}, and C_{66}) in Units of N/m, Young's Modulus (Y_{2D}), and Poisson Ratio (ν) of AsXX' Monolayers

2D AsXX'	C_{11}	C_{12}	C_{13}	C_{33}	C_{44}	C_{66}	Y_{2D}(N/m)	ν
AsSCl	54.07	17.53	0.04	0.16	17.75	18.27	48.39	0.31
AsSBr	46.97	15.46	0.08	0.23	12.96	15.76	41.87	0.33
AsSCl	42.41	14.50	0.45	1.56	12.54	13.96	37.44	0.33
AsSeCl	38.66	11.78	0.02	0.61	13.58	13.44	35.06	0.30
AsSeBr	37.98	11.76	0.04	0.09	14.84	13.44	34.34	0.31
AsSeI	33.99	10.51	0.04	0.12	13.97	11.74	30.73	0.31

simulations at room temperature for up to 5 ps within a supercell of size 4 × 4 × 1. To control the temperature in AIMD simulations, the Nose−Hoover thermostat[50] is employed under the NVT ensemble. The elastic constants and piezoelectric coefficients were calculated using finite difference method.[29,32]

For the computation of electronic transport properties, we used Rode's algorithm as implemented in the AMMCR package[51] in conjunction with VASP. We implement the 48 × 48 × 1 dense k-mesh for the sampling of the Brillouin zone. The electrical transport properties calculated by the CRTA (constant relaxation time approach) do not comprise any type of scattering mechanism that affects the experimental validation of theoretically anticipated results; therefore, various scattering mechanism models have been included in the calculations of the scattering rate. The lattice thermal conductivity of these monolayers is determined by the phono3py code.[52] Here, for the calculation of relaxation time, we adopt a supercell of size 4 × 4 × 1. The magneto-transport properties are investigated using the theory implemented in the AMMCR package.[51] To obtain charge transfer dynamics, we implemented a (NVT) microcanonical ensemble to perform MD simulation at 300 K with a supercell of size 3 × 3 × 1 carried out within the Hefei-NAMD code.[53]

3. RESULTS AND DISCUSSION

3.1. Structural Properties and Stability Analysis. The structure of asymmetric Janus AsXX' reveals that these monolayers possess a trigonal structure with a hexagonal unit cell having a $P3m1$ space group within a C_{3v} point group. The unit cell of these monolayers avails three atoms with an "As" atom jammed in between X and X' as depicted in Figure 1. As observed from Table S1, the presence of the lightest atoms, e.g., S and Cl, in AsSCl monolayers leads to the lowest relaxed lattice constant. The thickness of these monolayers increases due to the elongation of bonds between the As-X and As-X' sides, respectively. The widening of bond angles (α and β) arises as the electronegativity difference between these monolayers increases, and the electron is liberated around the most electronegative atom. The charge transfer ($\Delta\rho$) decreases as the atomic mass of chalcogens and halogens increases. From the average electrostatic potential curves, it is observed that the electrostatic potential difference ($\Delta\Phi$) decreases as the halogen atomic mass increases, as depicted in Figure S1. Note that the $\Delta\Phi$ is important for tailoring the electronic properties (bands alignments) for photovoltaic solar cells and photocatalytic water splitting.

3.1.1. Energetic Stability. The energetic stability of Janus AsXX' monolayers is evaluated by computing cohesive energy (E_C) by using the formula given as

$$E_C = \frac{[E_T(\mathrm{As}) + E_T(\mathrm{X}) + E_T(\mathrm{X}')] - [E_T(\mathrm{AsXX}')]}{3} \quad (1)$$

The terms E_T(As), E_T(X), and E_T(X') are the energies of single atoms corresponding to As, X, and X', respectively, and E_T (AsXX') is the total energy of AsXX' Janus monolayers. The lattice constants of the AsXX' monolayer decrease down the group that leads to larger bond lengths and hence the weak bond strength. The weakening of bonds results in the decrease in the cohesive energy (Table S1).

3.1.2. Dynamical and Thermal Stability. The dynamical stability of these monolayers is quantified by computing phonon dispersion spectra (Figure 1). The absence of negative frequency in Janus AsXX' monolayers suggested their dynamical stability. The phonon dispersion spectra of Janus AsXX' are composed of nine modes. Out of these, three are acoustic: ZA, TA, and LA, and the remaining represent optical modes. The ZA and LA/TA modes quantify the quadratic dispersion (p^2) and have linear dispersion near the Γ point according to the continuum elasticity theory. The phonon dispersion spectra of these monolayers shifted to the lower frequencies because of an increase in the atomic mass of constituent atoms. The lower frequencies correspond to the decrement of phonon group velocity of these monolayers. The overlapping of phonon band lines signifies the strong optical-acoustic phonon scattering.

Next, we evaluated the thermal stability of AsXX' monolayers by performing AIMD simulations. The smaller fluctuation of temperature around a constant level with respect to time steps confirms their thermal stability as depicted in Figure S2 and Figure S3. The atomic configuration of these monolayers remains undistorted even after heating systems at 300 and 800 K.

3.2. Mechanical and Piezoelectric Properties. After confirming stability, we compute the mechanical properties in terms of nonzero elastic constants (C_{jk}), Young's modulus (Y_{2D}), and Poisson ratio (ν) as tabulated in Table 1. The mechanical stability is confirmed by Born and Huang criteria[54] given as

$$C_{11} > |C_{12}| \text{ and } C_{66} = \frac{C_{11} - C_{12}}{2} > 0 \quad (2)$$

Further, these monolayers also exhibit the Mouhat and Coudert criteria,[54] according to which the four necessary conditions for the stability of the structures are $C_{11} > |C_{12}|$, $2C_{13}^2 < C_{33}(C_{11} + C_{12})$, $C_{44} > 0$, and $C_{66} > 0$. The Janus AsXX' monolayers fulfill these criteria, which indicates their mechanical stability. The stiffness of these monolayers is characterized in terms of Young's modulus, given as

https://doi.org/10.1021/acsomega.4c02874
ACS Omega 2024, 9, 33723−33734

$$Y_{2D} = \frac{(C_{11}^2 - C_{12}^2)}{C_{11}} \quad (3)$$

The elongation of bonds between the atoms leads to the reduction of Young's modulus as we move to AsSeI from AsSCl monolayers. The fraction of the transverse strain to the axial strain delivers the Poisson ratio ($\nu = C_{12}/C_{11}$). The computed ν values are in the range 0.21−0.31 (Table 1). The Poisson's ratio of Janus AsXX' monolayers fulfills the criteria of Frantsevich rule, which confirms the brittle nature of these monolayers.[55]

After discussing the various elastic coefficients, next, we analyze the piezoelectric behavior of these monolayers in terms of piezoelectric strain and stress coefficients. Piezoelectricity is defined as electromechanical coupling between external stress and intrinsic electrical polarization, which arises due to the absence of inversion symmetry in Janus monolayers.[56−58] The piezoelectric behavior of 2D monolayers is expressed in terms of isothermal piezoelectric coefficients,[58] which are known as piezoelectric stress coefficients (e_{11} and e_{31}) and piezoelectric strain coefficients (d_{11} and d_{31}).[57,58] These piezoelectric stress and strain coefficients are different for the direct piezoelectric effect (DPZ) and the reverse piezoelectric effect (RPZ). In DPZ, electrical polarization arises due to externally applied stress, while in RPZ, when an external electric field (EF) is applied to the system, it deforms the system.

The piezoelectric strain coefficient (e_{xyz}) for the 2D system is given as the combination of electronic and ionic part:

$$e_{xyz} = e_{xyz}^{\text{electronic}} + e_{xyz}^{\text{ionic}} \quad (4)$$

For the direct polarization effect and reverse polarization effect, the strain coefficient of piezoelectricity is given as

$$e_{ijk} = \left(\frac{\partial P_i}{\partial \varepsilon_{jk}}\right)_{E,T}, \left(\text{forDPZ}\right) \quad (5)$$

$$e_{ijk} = \left(\frac{\partial P_i}{\partial E_{jk}}\right)_{\varepsilon,T}, \ (\text{forRPZ}) \quad (6)$$

where P_i and σ_{jk} correspond to the electric polarization and stress tensor, respectively.

The piezoelectric strain coefficient e_{ij} is demonstrated by using Voigt notation given as

$$e_{ij} = d_{ik}C_{kj} \quad (7)$$

where C_{kj} stands for elastic tensor given as

$$C = \begin{pmatrix} C_{11} & C_{12} & C_{13} & \cdots\cdots & \cdots\cdots & \cdots\cdots \\ C_{12} & C_{11} & C_{13} & -C_{14} & \cdots\cdots & \cdots\cdots \\ C_{31} & C_{31} & C_{33} & \cdots\cdots & \cdots\cdots & \cdots\cdots \\ C_{14} & -C_{14} & \cdots\cdots & C_{44} & \cdots\cdots & \cdots\cdots \\ \cdots\cdots & \cdots\cdots & \cdots\cdots & & C_{44} & C_{14} \\ \cdots\cdots & \cdots\cdots & \cdots\cdots & \cdots\cdots & C_{14} & \dfrac{C_{11}-C_{12}}{2} \end{pmatrix} \quad (8)$$

Further, these elastic stiffness coefficients are elaborated in elastic strain coefficients, which are represented as

$$C_{11} = C_{22} = \frac{1}{S}\frac{\partial^2 E}{\partial \varepsilon_{11}^2} \text{ and } C_{12} = \frac{1}{S}\frac{\partial^2 E}{\partial \varepsilon_{11}\partial \varepsilon_{22}} \quad (9)$$

where S is the area of the unit cell.

Due to the C_{3v} symmetry in Janus monolayers and as consequences of Voigt notation, the piezoelectric stress (e_{ij}) and strain (d_{ik}) coefficients given as

$$e_{ij} = \begin{bmatrix} e_{11} & -- & ---- & e_{15} & -e_{22} \\ -e_{22} & e_{22} & -- & e_{15} & -- & -- \\ e_{31} & e_{31} & e_{33} & -- & -- & -- \end{bmatrix} \quad (10)$$

$$d_{jk} = \begin{bmatrix} d_{11} & -- & ---- & d_{15} & -d_{22} \\ -d_{22} & d_{22} & -- & d_{15} & -- & -- \\ d_{31} & d_{31} & d_{33} & -- & -- & -- \end{bmatrix} \quad (11)$$

where "--" stands for zero values. These piezoelectric tensors are reduced to second order from third order and hence are represented by 3 × 6 matrices.

By performing symmetry analysis, the number of piezoelectric stress and strain coefficient reduces as[32,59]

$$e = \begin{pmatrix} e_{11} & -e_{11} & 0 \\ 0 & 0 & -e_{11} \\ e_{31} & e_{31} & 0 \end{pmatrix} \quad (12)$$

$$d = \begin{pmatrix} d_{11} & -d_{11} & 0 \\ 0 & 0 & -2d_{11} \\ d_{31} & d_{31} & 0 \end{pmatrix} \quad (13)$$

The noncentrosymmetric behavior and broken inversion symmetry in Janus monolayers give rise to the piezoelectric coefficients and these coefficients are direction-dependent. The d_{11} or in-plane piezoelectric coefficients arise due to the arousal of in-plane electrical polarization when the same mechanical stress is applied along the same direction. Further, the d_{31} or out-of-plane (z-direction) electrical polarization arises when mechanical stress is applied along the x-direction. For the unstrained system, the in-plane and out-of-plane piezoelectric tensor is given as[60,61]

$$d_{11} = \frac{e_{11}}{C_{11} - C_{12}}, \ d_{31} = \frac{e_{31}}{C_{11} + C_{12}} \quad (14)$$

The values of C_{11}, C_{12}, d_{11}, d_{31}, e_{11}, and e_{31} are listed in Table 1 and Table 2. Note that the out-of-plane piezoelectric coefficient (d_{31}) reported for other monolayers in the literature

Table 2. Piezoelectric Stress Coefficients (e_{11} and e_{31}) and Corresponding Piezoelectric Strain Coefficients (d_{11} and d_{31}), Respectively, of Janus AsXX' Monolayers[a]

2D monolayers	e_{11} (C/m)	e_{31} (C/m)	d_{11}(pm/V)	d_{31}(pm/V)
AsSCl	10.42	0.009	28.50	0.013
AsSBr	12.90	−0.193	40.94	−0.31
AsSI	14.56	−0.448	52.17	−0.79
AsSeCl	3.65	0.076	13.58	0.15
AsSeBr	5.61	−0.066	21.40	−0.13
AsSeI	7.88	−0.224	33.55	−0.50

[a]Note that e_{11} and e_{31} are in the power of 10^{-10}.

https://doi.org/10.1021/acsomega.4c02874
ACS Omega 2024, 9, 33723−33734

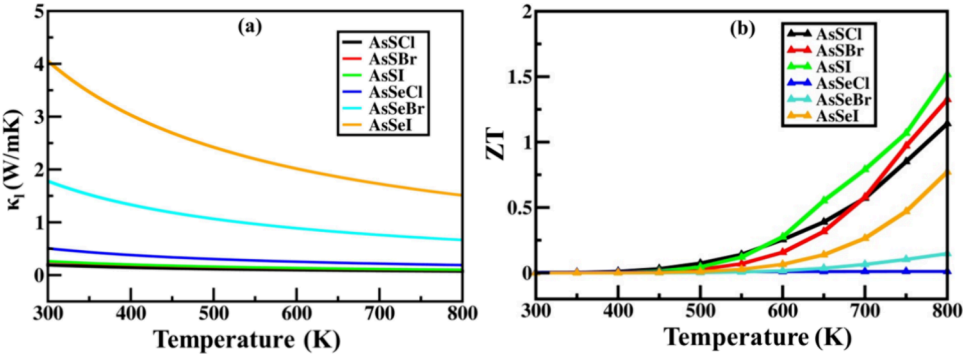

Figure 2. (a) Lattice thermal conductivity and (b) thermoelectric performance of 2D Janus AsXX' monolayers as a function of temperature.

is as follows: MoSSe (0.29 pm/V),[61] MoSTe (0.4 pm/V),[60] 1H-WSO (0.4 pm/V),[62] BiSF (−0.33 pm/V),[32] BiSCl (−0.29 pm/V),[32] and BiSBr (−0.41 pm/V)[32] monolayers. The strong out-of-plane piezoelectricity of Janus AsXX' monolayers makes them potential candidates for piezoelectric devices. When the piezoelectric material is deformed corresponding to the strain, it generates an electric field that enhances the heat transfer and helps the thermoelectric device to maintain favorable temperature. So, next, we discuss the thermoelectric properties of Janus AsXX' monolayers.

3.3. Thermoelectric Properties. *3.3.1. Lattice Thermal Conductivity.* The phonon transport properties play an important role in the calculation of the lattice thermal conductivity (LTC) (κ_l). The κ_l values of Janus AsXX' monolayers are characterized in terms of phonon transport variables such as phonon group velocities (v_g), Gruneisen parameters (γ), etc. The (κ_l) at temperature T is formulated as

$$\kappa_{l,j} = \sum\sum C_p \nu_{g,j}^2(\lambda, q')\tau(\lambda, q') \quad (15)$$

where C_p represents the specific heat capacity.

Janus AsXX' monolayers exhibit a decrease in lattice thermal conductivity as temperature increases, suggesting Umklapp anharmonic interactions. The calculated values of LTC at 300 K range from 0.61 to 1.83 W/mK for 2D Janus AsXX' (Figure 2a). The calculated value of lattice thermal conductivity is lower than those of BiOCl (3 W/mK),[63] PdSTe (5.45 W/mK), and PdSeTe (4.02 W/mK)[20] and comparable with those of BiTeCl (1.46 W/mK),[27] BiTeBr (1.47),[26] and AsTeCl (0.92 W/mK)[21] monolayers.

Next, we computed the phonon's group velocities for different modes as

$$v_g(\lambda, q^*) = \frac{\partial\omega(\lambda, q^*)}{\partial q} \quad (16)$$

The maximum value of LA, ZA, and TA modes reaches up to 40 Km/s. The phonon group velocities of Janus AsXX' monolayers reach up to 40 Km/s (Figure S4). The lattice thermal conductivity is directly linked with phonon group velocity, as the lower the value of phonon group velocity, the lower is the lattice thermal conductivity.

Furthermore, the κ_l can also be elaborated in terms of a dimensionless quantity γ formulated as

$$\gamma_{\lambda,q} = \frac{-V}{w_{\lambda,q}}\frac{\partial\omega_{\lambda,q}}{\partial V} \quad (17)$$

The γ character describes the anharmonic interaction in the crystal structure. The greater the value of γ, the higher the phonon−phonon scattering is, leading to the lower phonon relaxation time value. The calculated value of γ reaches up to 40, corresponding to the Janus AsXX' monolayer. The ZA mode of γ contributes more than that of the TA and LA mode. From Figure S5, it is observed that the contribution of optical modes is much less than acoustic modes, which indicates that κ_l majorly arises due to the anharmonic acoustic scattering of phonons.[64] The high value of γ and the low value of v_g are responsible for the low value of the lattice thermal conductivity.

3.3.2. Electronic Transport Properties. Relaxation time calculation using the RTA approach has several limitations. Scattering rate calculation by the RTA approach is unsuitable for an inelastic scattering mechanism. To overcome RTA limitation, we employed Rode's algorithm[51] to include various scattering mechanisms for the appropriate relaxation time approximation. Thus, the momentum-dependent relaxation time is calculated, including eight different kinds of scattering, i.e., ionized impurity scattering ($\tau_{Ii}(k)$), polar optical phonon scattering due to longitudinal phonon ($\tau_{Pop}(k)$), dislocation scattering ($\tau_{Dis}(k)$), alloy scattering ($\tau_{Alloy}(k)$), intravalley scattering ($\tau_{Iv}(k)$), piezoelectric scattering ($\tau_{Pz}(k)$), acoustic deformation scattering ($\tau_{Ac}(k)$), and neutral impurity scattering ($\tau_{Ni}(k)$), in the calculations. These scattering mechanisms are expressed as[65]

$$\frac{1}{\tau(k)} = \frac{1}{\tau_{Ii}(k)} + \frac{1}{\tau_{Ac}(k)} + \frac{1}{\tau_{Pz}(k)} + \frac{1}{\tau_{Dis}(k)} + \frac{1}{\tau_{Alloy}(k)} + \frac{1}{\tau_{Iv}(k)} + \frac{1}{T_{Ni}(k)} + \frac{1}{\tau_{Pop(k)}} \quad (18)$$

Out of these eight scattering mechanisms, τ_{Pop}, τ_{Ac}, and τ_{Pz} play the most significant role. Pop (polar optical polar) scattering predominates in regions with higher temperatures or near room temperature. The acoustic deformation potential scattering arises from the scattering of electrons from acoustic phonons. The contribution of piezoelectric scattering in Janus monolayers arises from the presence of an in-built intrinsic electric field. We have taken the piezoelectric coefficient from Table 2 for the calculations. The scattering rates of Janus AsXX' monolayers are mentioned in Figure S6a. Note that the inclusion of these scattering models provides more consistency with experimental results.[51] For calculating electronic transport properties, we have accounted for the relaxation time incorporated with various scattering mechanisms rather than

https://doi.org/10.1021/acsomega.4c02874
ACS Omega 2024, 9, 33723−33734

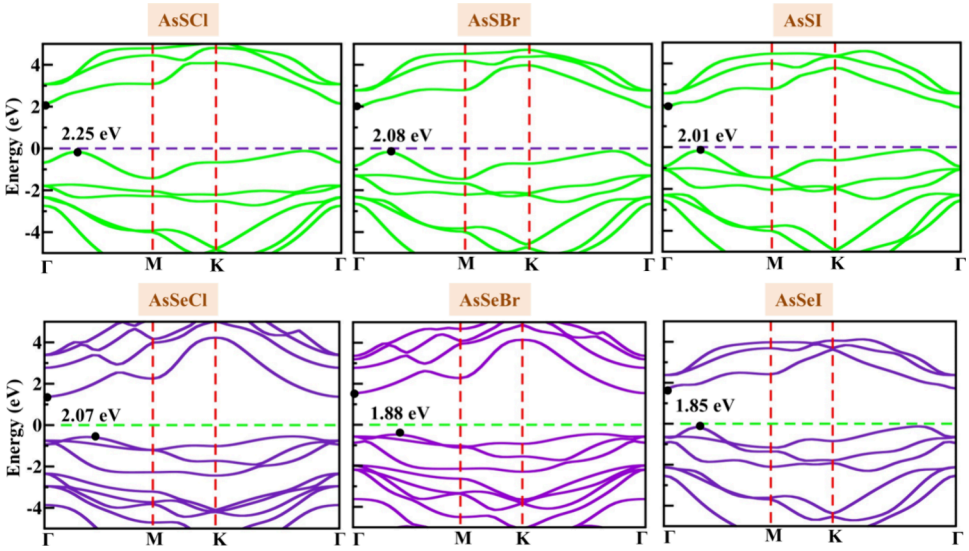

Figure 3. Band structure of AsXX' monolayers using the HSE06 level of theory.

the constant relaxations time approach. For Janus AsXX' monolayers, the computed value of relaxation time lies in the range of 0.008−0.09 ($\times 10^{-14}$ s).

Next, we implement a momentum-dependent scattering mechanism and semiclassical Boltzmann transport theory within the BoltzTraP code to calculate electronic transport properties.[66] The Seebeck coefficient (S), electronic thermal conductivity (κ_e), electrical conductivity (σ), and power factor (P) of Janus AsXX' monolayers play an essential role in the calculation of (zT). We have calculated the Seebeck coefficient (S) in the temperature range of 300 to 800 K as depicted in Figure S6b. The σ values of these monolayers also increase with temperature (Figure S6c). To compute κ_e, Wiedemann−Franz law is given as

$$\kappa_e = L\sigma T \tag{19}$$

where L is the Lorentz number. For semiconductors, the fixed value of L is 2.44 × 10^{-8} WΩK^{-2}.[67] Since L varies from material to material, so we have taken the Seebeck coefficient-dependent L values given as[68]

$$L = 1.5 + \exp\left(\frac{-|S|}{116}\right) \tag{20}$$

Here, S is the value of the Seebeck coefficient in the units of μV/K. Different S corresponds to different L. The calculated values of electronic thermal conductivity at 800 K are 16, 13, 10, 80, 32, and 20 W/mK for AsSCl, AsSBr, AsSI, AsSeCl, AsSeBr, and AsSeI, respectively. By the integrated effect of σ and S, we calculate the power factor (P), formulated as

$$P = S^2\sigma \tag{21}$$

The power factor of Janus AsSX' monolayers is higher than that of AsSeX' monolayers (Figure S6d). The vast difference between the power factor affects thermoelectric performance of these monolayers. The higher value of the power factor of the AsSI monolayer leads to its higher value of thermoelectric performance.

By the integrate effect of κ_l and P, the thermoelectric performance of Janus AsXX' monolayers is formulated as[69]

$$zT = \frac{S^2\sigma T}{\kappa_e + \kappa_l} \tag{22}$$

The thermoelectric performance gradually increases with temperature because of the reduction of lattice thermal conductivity. Among various Janus AsXX' monolayers, AsSI exhibits high thermoelectric performance at 800 K due to low lattice thermal conductivity and high thermoelectric transport properties (Figure 2b). The comparison of the thermoelectric performance of Janus AsXX' monolayers with the other 2D monolayers is made in Table S2. From this comparison, it is clear that the Janus AsXX' monolayer acts as a potential candidate in the field of thermoelectrics at higher temperatures (800−900 K).

3.4. Optoelectronics Properties. To study the electronic band structure of Janus AsXX' monolayers, we implement different methods, i.e., GGA, HSE06, and G_0W_0. The calculated value of the band gap using these methods is tabulated in Table S3. Janus AsXX' monolayers exhibit an indirect bandgap in the vicinity of Γ and M high symmetry points. Due to the bond elongation, the bandgap decreases as depicted in Figure 3. The total density of states (TDOS) of AsXX' monolayers is also depicted in Figure S7. On analyzing the partial density of states (PDOS) of these monolayers, it has been observed that the valence states near the Fermi level are dominated by As atoms while conduction states near the Fermi level show strong hybridization between chalcogen and halogen atoms (Figure S8).

To study the light-harvesting ability of these monolayers, we computed the optical absorbance spectra of AsXX' monolayers using G_0W_0-BSE methods.[70] The optical absorbance of these monolayers are computed as[71]

$$A(\omega) = \frac{\omega}{c} L\varepsilon_1(\omega) \tag{23}$$

$\varepsilon_1(\omega)$ is the imaginary part of the dielectric function, and L is the length of the unit cell in the Z-direction. The $A(\omega)$ of AsXX' monolayers lie in the UV−visible region with the first most prominent peak in the visible region (Figure 4). We computed excitonic binding energy of photogenerated charge carriers to analyze their photoexcitation. The excitonic binding energy (E_b) is formulated as

https://doi.org/10.1021/acsomega.4c02874
ACS Omega 2024, 9, 33723−33734

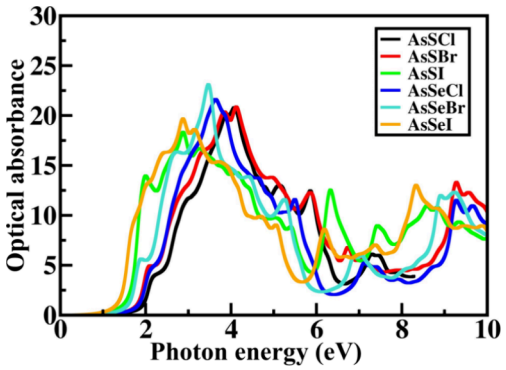

Figure 4. Optical absorbance spectra of AsXX' monolayers using the GW-BSE level of theory.

$$E_b = E_{QP} - E_{OPTICAL} \quad (24)$$

where E_{QP} and $E_{OPTICAL}$ stand for the energies of the quasi-particle direct bandgap and the first most prominent peak, respectively. The computed value of the excitonic binding energy is listed in Table S3. The excitonic binding energy decreases as the electronegativity difference between the constituent atoms decreases. The excitonic binding energy of AsXX' monolayers is lower than MgO (2.49 eV),[72] BeN_2 (1.07 eV),[73] and MoS_2 (1.1 eV).[74] These results indicate that these monolayers have extraordinary capability in light-harvesting devices. The lower excitonic binding energy facilitates the separation of electron−hole pairs and reduces the electron−hole recombination before they participate in redox reaction. Efficient charge separation is helpful for achieving high photocatalytic activity and thus improves the overall performance of the photocatalyst.

Considering the semiconducting nature and excellent light-harvesting capabilities, we have designed six AsSeI-based type-II heterostructures having minimum lattice mismatch for photovoltaic solar cells (Figure S9 and Table S4). The lower lattice mismatch with minimum conduction band offset in the case of AsSeI/AsTeI monolayers gives rise to a high value of power conversion efficiency (PCE) up to ∼19% (Table S5). The detailed discussion of the proposed heterostructure for solar cells is given in the SI.

Next, we consider the effect of magnetic field and electric field on charge carriers in terms of magneto-transport properties and carrier mobility. The magneto-transport properties are incorporated with Hall conductivity (σ_H) and Hall factor (r) (Figure S10). The detailed discussion of magneto-transport properties is given in the SI. Furthermore, the carrier mobility of the Janus AsXX' monolayers by including various scattering mechanisms is depicted in Figure 5. We employed Matthiessen's rule for the calculation of temperature-dependent carrier mobility (μ), which is formulated as

$$\frac{1}{\mu} = \frac{1}{\mu_{Ac}} + \frac{1}{\mu_{Pz}} + \frac{1}{\mu_{Pop}} \quad (25)$$

where μ_{Ac}, μ_{Pz}, and μ_{Pop} represent the carrier mobility arising due to the acoustic, piezoelectric, and polar-optical contributions, respectively. Here, we incorporate only three types of scattering because, in the case of Janus monolayers, these scattering mainly plays an important role. AC scattering arises due to the coupling of electrons with an acoustic phonon, piezoelectric scattering in Janus monolayer arises due to the presence of an in-built electric field, and Pop scattering arises due to the interaction of electron with optical phonons, and it is the dominant scattering mechanism near the room temperature or high-temperature region.[33] The carrier mobility of these monolayers decreases with T because as the T increases, the electrons scatter more; thus, their mobility decreases. The scattering rate of AsSCl charge carriers is less as compared to other AsXX' monolayers; this will lead to a higher value of carrier mobility for the AsSCl monolayer (∼10,000 $cm^2V^{-1}s^{-1}$ at room temperature). Carrier mobility of charge carriers plays an important role in various applications such as photovoltaic solar cells and photocatalytic water splitting.

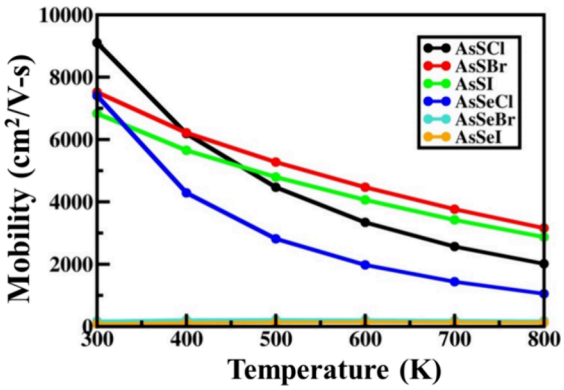

Figure 5. Carrier mobility of AsXX' Janus monolayers as a function of temperature.

3.5. Photocatalytic Properties. Apart from the photovoltaic solar cell, solar energy also plays an important role in water splitting. Due to the excellent light-harvesting ability of Janus AsXX' monolayers, we compute the photocatalytic properties of these monolayers. Of these six monolayers, only AsSCl, AsSBr, and AsSeI monolayers possess suitable band alignment for water splitting. As shown in Figure 6a, the valence band position from the halogen side and conduction band position from the chalcogen side properly engulf the redox potential of water, which makes hydrogen evolution reaction (HER) and oxygen evolution reaction (OER) feasible for these monolayers. Note that the positions VBM and CBM with respect to the redox potential are important. Only those VBM/CBM take part in redox reaction, which properly engulf the redox potential of water. In the case of the AsSCl monolayer, the VBM and CBM of both the surfaces properly engulf the redox potential of water, but we choose the VBM of chalcogen and CBM of halogen because these lie near the redox potential of water.

The schematic of photoexcitation is illustrated in Figure 6a for AsSCl, AsSBr, and AsSeI interfaces, where 1, 2, and 3 represent the electron dynamics, holes dynamics, and electron−hole recombination dynamics, when an electron and hole pair is generated after photoexcitation. The electron transfer takes place between the higher VBM to lower VBM, while hole transfer takes from the lower VBM of one surface to the higher VBM of other surface. Further the recombination of photogenerated charge carriers takes place between the VBM and CBM of different surfaces near the redox potential of water. By implementing the method proposed by Chen and Wang,[75] we further analyzed the photocatalytic stability of these monolayers in aqueous solution (SI). As depicted in Figure 6b, hydrogen evolution reaction (HER) and oxygen evolution reaction (OER) are two- and four-step mechanisms.

https://doi.org/10.1021/acsomega.4c02874
ACS Omega 2024, 9, 33723−33734

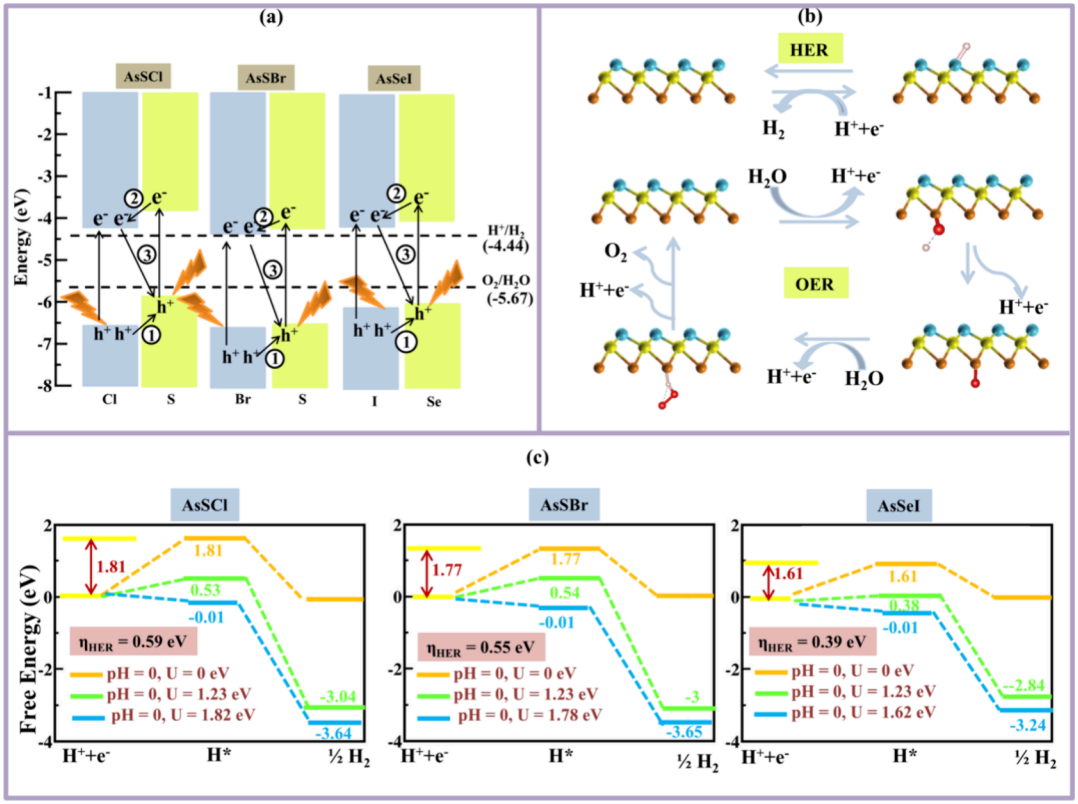

Figure 6. (a) Computed band alignments of AsXX' monolayers at the HSE06 level of theory. 1, 2, and 3 represent the electron, hole, and electron−hole recombination pathways, respectively. (b) Configuration of adsorption of atomic species for hydrogen evolution reaction and oxygen evolution reaction and (c) Gibbs free energy pathways for hydrogen evolution reaction that corresponds to AsSCl, AsSBr, and AsSeI monolayers. The rate-limiting potentials for AsSCl, AsSBr, and AsSeI are 1.81 1.77, and 1.61 eV, respectively. The external potential (η_{OER}) required to make OER feasible is also shown.

3.5.1. Gibbs Free Energy Profile. Gibbs free energy profiles are another important aspect in analyzing the hydrogen and oxygen evolution mechanisms. The various parameters such as zero point energy (ZPE) and entropy ($T\Delta S$) are required to calculate the Gibbs free energy of these monolayers (Table S6). The detailed calculation of Gibbs free energy of these monolayers is given in SI. The computed values of photogenerated electron potential (U_e = energy difference of reduction potential of H^+/H_2 and conduction band minima) are 0.08 0.01, and 0.19 eV corresponding to AsSCl, AsSBr, and AsSeI monolayers, respectively. Due to the less value of photogenerated electron potential, we take the standard value of U_e, i.e., 1.23 eV, in the Gibbs free energy plot.[76] Therefore, external potentials of 0.59, 0.55, and 0.39 eV corresponding to AsSCl, AsSBr, and AsSeI monolayers, respectively, are required to make HER feasible in these monolayers as depicted in Figure 6c.

The computed values of photogenerated hole potential (U_h = energy difference of reduction potential of H^+/H_2 and valence band maxima) are 1.66, 2.0, and 2.17 eV corresponding to AsSCl, AsSBr, and AsSeI monolayers, respectively. For the OER reaction, external potentials of 1.14 0.37, and 0.36 eV are required to make the reaction feasible, as depicted in Figure S11. Note that previous studies have shown that the strain engineering[77] and defect engineering[78] methods can improve the photocatalytic performance by reducing the external potential required to make HER/OER feasible in 2D monolayers. Therefore, we have aligned the band positions of AsSCl, AsSBr, and AsSeI monolayers strained at 1, 2, 3, and 4%. After applying strain, only AsSeI at 1 and 2% exhibits a proper band alignment for water splitting (Figure S12). The calculated values of photogenerated electron potential for hydrogen reduction and photogenerated hole potential for water oxidation are given in Table S7. The Gibbs free energy profiles of AsTeI for HER and OER at different values of strain are depicted in Figure S13 and Figure S14, respectively. The extra potential (η_{HER}) required to trigger the HER spontaneously increases with strain, whereas the extra potential (η_{OER}) required to make the OER spontaneous show decrease at 2% of strain. It indicates that strain engineering can be adopted as a potential tool to improve the photocatalytic performance of 2D monolayers.

3.5.2. Solar-to-Hydrogen Conversion Efficiency. Next, the solar-to-hydrogen (η_{STH}) conversion efficiency of these monolayers are formulated as[79]

$$\eta_{STH} = \eta_{Abs} \times \eta_{Cu} \tag{26}$$

where η_{Abs} and η_{Cu} stand for the absorption efficiency and carrier utilization efficiency. η_{Abs} is given as

$$\eta_{Abs} = \frac{\int_{E_g}^{\infty} E(\hbar\omega)\, d(\hbar\omega)}{\int_{0}^{\infty} E(\hbar\omega)\, d(\hbar\omega)} \tag{27}$$

Next, the η_{CU} is calculated as

https://doi.org/10.1021/acsomega.4c02874
ACS Omega 2024, 9, 33723−33734

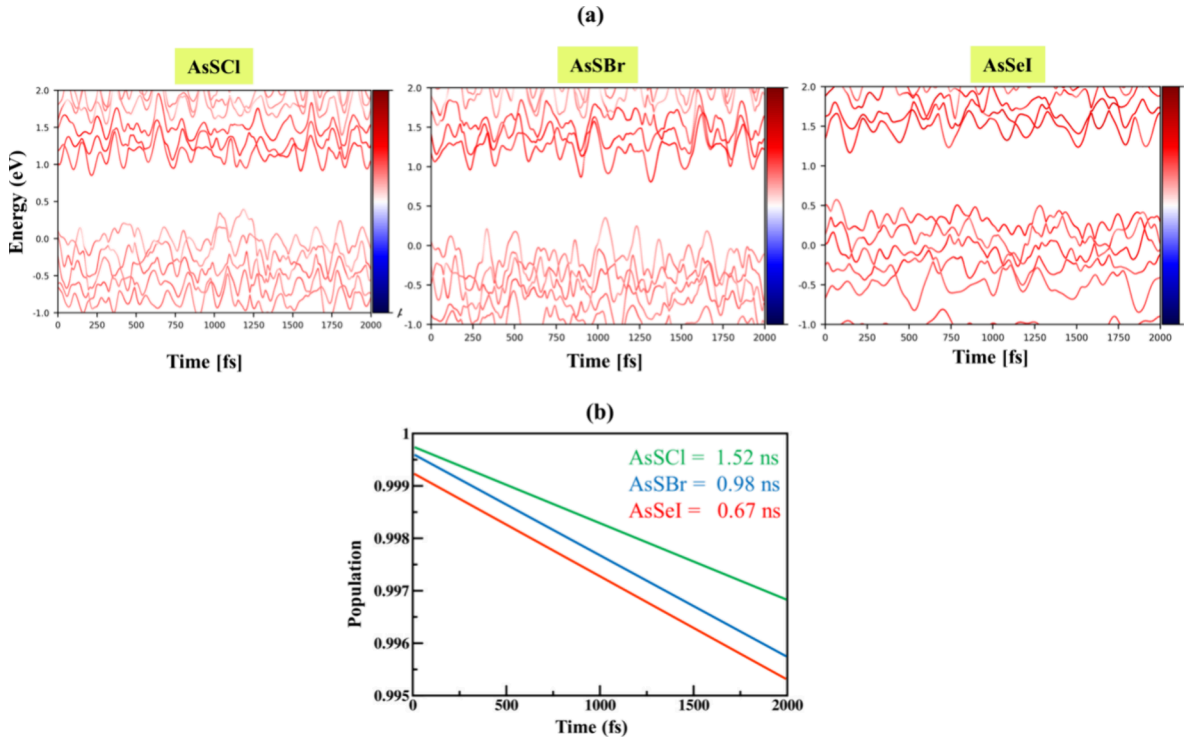

Figure 7. (a) Energy evolution of Kohn–Sham (KS) states near the Fermi level and (b) electron–hole recombination rate for the photocatalytic water splitting process of AsSCl, AsSBr, and AsSeI monolayers.

$$\eta_{CU} = \Delta G \times \frac{\int_{E}^{\infty} P(\hbar\omega)\, d(\hbar\omega)}{\int_{E_g}^{\infty} P(\hbar\omega)\, d(\hbar\omega)} \tag{28}$$

where E is the photon energy used for the photocatalytic mechanism.

The calculated values of η_{Abs} (η_{Cu}) for AsSCl, AsSBr, and AsSeI monolayers are 56.78% (44.86%), 59.17% (45.76%), and 61.86% (48.89%), respectively. The presence of an in-built intrinsic electric field facilitates the photogenerated charge carriers in the form of potential difference (ΔV); therefore, the corrected solar-to-hydrogen efficiency (η'_{STH}) is formulated as

$$\eta'_{STH} = \eta_{STH} \times \frac{\int_{0}^{\infty} E(\hbar\omega)\, d(\hbar\omega)}{\int_{0}^{\infty} E(\hbar\omega)\, d(\hbar\omega) \times \Delta V \int_{E_g}^{\infty} \frac{E(\hbar\omega)\, d(\hbar\omega)}{\hbar\omega}} \tag{29}$$

The calculated values of η'_{STH} are ~12, 16, and 19%, respectively. These monolayers' η'_{STH} fulfilled the 10% efficiency target for the commercial production of hydrogen. The comparison of the corrected solar to hydrogen conversion efficiency with other 2D monolayers is listed in Table S8. For in-depth insights into the photocatalytic water splitting, we compute the charge transfer behavior of these monolayers in terms of electron transfer, hole transfer, and recombination rate.

3.5.3. Charge Transfer Dynamics. Next, we study the charge transfer dynamics of AsSCl, AsSBr, and AsSeI monolayers in the context of photocatalytic water splitting. The recombination rate of the charge carriers affects the corrected solar-to-hydrogen conversion efficiency. To quantitatively analyze the lifetime of photogenerated electron–hole pair recombination, we first demonstrate the evolution of the state populations. By evaluating the time-dependent Kohn-Sham (TDKS) equation at configuration $R(T)$, the TDKS orbitals $\psi_E(r, T)$ (Figure 7a) is expressed as[53]

$$\psi_E(r, T) = \sum_k C_k(T)\phi_k(r, R(T)) \tag{30}$$

Electron–phonon coupling plays an important role in the charge carrier recombination process. In nonadiabatic molecular dynamics simulations, the photogenerated charge carrier recombination rate depends upon the decoherence time (D_T) and NACs (nonadiabatic coupling) time.[53] The recombination rate of photogenerated charge carriers mainly depends on NACs: the smaller the NACs, the smaller the recombination rate. The phonon exciton and electron–phonon coupling gave the D_T and NACs. The nonadiabatic coupling of charge carriers is given as

$$d_{xy} = \langle \psi_x | \frac{\partial}{\partial t} | \psi_y \rangle = \frac{\langle \psi_x | \nabla_r H | \psi_y \rangle}{\varepsilon_y - \varepsilon_x} \dot{r} \tag{31}$$

where $\dot{r}$ is the velocity of the nuclei. NACs are calculated by electron–phonon coupling elements ($\langle \psi_x | \nabla_r H | \psi_y \rangle$), energy gap ($\varepsilon_y - \varepsilon_x$), and velocity ($\dot{r}$). The computed value of nonadiabatic coupling time is Table S8.

Further, we calculate the electron transfer rate (τ_e) and hole transfer rate (τ_h) corresponding to steps 1 and 2 (Figure 6a) for AsSCl, AsSBr, and AsSeI Janus monolayers. The electron transfer rate is higher than the hole transfer rate as listed in Table S9. The electron–hole recombination rate (τ) for the full exponential decay process is formulated as[80]

$$P(T) = \exp\left(\frac{-T}{\tau}\right) \tag{32}$$

https://doi.org/10.1021/acsomega.4c02874
ACS Omega 2024, 9, 33723–33734

The calculated electron hole recombination rate values are 1.52, 0.98, and 0.67 ns corresponding to AsSCl, AsSBr, and AsSeI monolayers, respectively, as depicted in Figure 7b. Note that the recombination rate value of other 2D monolayers are Ga_2SeTe (51.5 ns),[81] In_2SeTe (61.1 ns),[81] In_2STe (72.8 ns),[81] and $PtSe_2$ (>10 ns).[82]

4. CONCLUSIONS

In this study, we computed the piezoelectric, thermoelectric, and photocatalytic properties of 2D Janus AsXX' monolayers. The positive phonon dispersion spectra, AIMD curves, and nonzero elastic coefficients confirm their dynamical, thermal, and mechanical stability, respectively. These monolayers possess strong out-of-plane piezoelectric coefficients. Using various scattering models, the scattering rate has been estimated to obtain the thermoelectric performance of these monolayers in terms of zT, which lies in the range of 0.09 to 1.51 at 800 K. These monolayers exhibit an indirect band gap with high carrier mobility and strong visible light optical absorption spectra. The power conversion efficiency of AsSeI-based type-II heterostructures has been shown to reach up to 19%. Further, AsSCl, AsSBr, and AsSeBr monolayers exhibit suitable band alignment for water splitting. AsSCl, AsSBr, and AsSeI monolayers can be potential candidates for water splitting with solar-to-hydrogen conversion efficiencies 12, 16, and 19%, respectively. Further, the extra potential (η_{HER}) required to trigger the HER spontaneously increases as the strain increases, whereas the extra potential (η_{OER}) required to make the OER spontaneous show a decrease at 2% of strain. The calculated values of electron−hole recombination rates are 1.56, 0.98, and 0.67 ns corresponding to AsSCl, AsSBr, and AsSeI monolayers, respectively. These findings indicate that Janus arsenic chalcohalide monolayers can act as potential candidates for energy-harvesting applications.

■ ASSOCIATED CONTENT

Supporting Information

The Supporting Information is available free of charge at https://pubs.acs.org/doi/10.1021/acsomega.4c02874.

Structural parameters; electrostatic potential plots; AIMD simulation plots at 300 and 800 K; group velocity plots; Gruneisen parameters plots; plots of scattering rate, Seebeck coefficient, and electrical conductivity; thermoelectric performance (zT); DOS and PDOS plots; photovoltaic solar cell properties; magneto-transport properties; Gibbs free energy OER profiles; solar-to-hydrogen conversion efficiency and charge transfer dynamics (PDF)

■ AUTHOR INFORMATION

Corresponding Author

Ashok Kumar − *Department of Physics, Central University of Punjab, Bathinda 151401, India;* orcid.org/0000-0003-3636-0502; Email: ashokphy@cup.edu.in

Author

Poonam Chauhan − *Department of Physics, Central University of Punjab, Bathinda 151401, India*

Complete contact information is available at: https://pubs.acs.org/10.1021/acsomega.4c02874

Notes

The authors declare no competing financial interest.

■ ACKNOWLEDGMENTS

P.C. thanks the CSIR for providing financial support in the form of a senior research fellowship (SRF). We acknowledge the helpful discussion with Dr. Jaspreet Singh. The results presented in this work were obtained using the computational resources at the Department of Physics of Central University of Punjab.

■ REFERENCES

(1) Shi, X.-L.; Zou, J.; Chen, Z.-G. Advanced thermoelectric design: from materials and structures to devices. *Chem. Rev.* **2020**, *120* (15), 7399−7515.

(2) Sivaraman, S. K.; Raman, S. P.; Karthik, R.; Subair, T.; Ajai Krishnan, U.; Nair, S. S.; Shaji, S.; Tiwary, C. S.; Anantharaman, M. R. Lead-Free Piezoelectric Energy Harvester Based on 2D Bismuth Titanate. *ACS Appl. Mater. Interfaces* **2023**, 57192.

(3) Sezer, N.; Koç, M. A comprehensive review on the state-of-the-art of piezoelectric energy harvesting. *Nano energy* **2021**, *80*, No. 105567.

(4) Nishioka, S.; Osterloh, F. E.; Wang, X.; Mallouk, T. E.; Maeda, K. Photocatalytic water splitting. *Nat. Rev. Methods Primers* **2023**, *3* (1), 42.

(5) Yang, M.; Hu, Y.; Zheng, S.; Liu, Z.; Li, W.; Yan, F. Integrated Moist-Thermoelectric Generator for Efficient Waste Steam Energy Utilization. *Adv. Sci.* **2022**, 2206071.

(6) Sherrell, P. C.; Fronzi, M.; Shepelin, N. A.; Corletto, A.; Winkler, D. A.; Ford, M.; Shapter, J. G.; Ellis, A. V. A bright future for engineering piezoelectric 2D crystals. *Chem. Soc. Rev.* **2022**, *51* (2), 650−671.

(7) Chu, Y.; Zhong, J.; Liu, H.; Ma, Y.; Liu, N.; Song, Y.; Liang, J.; Shao, Z.; Sun, Y.; Dong, Y.; Wang, X.; Lin, L. Human pulse diagnosis for medical assessments using a wearable piezoelectret sensing system. *Adv. Funct. Mater.* **2018**, *28* (40), 1803413. Cheng, Y.; Ma, Y.; Li, L.; Zhu, M.; Yue, Y.; Liu, W.; Wang, L.; Jia, S.; Li, C.; Qi, T.; Wang, J.; Gao, Y. Bioinspired microspines for a high-performance spray $Ti_3C_2T_x$ MXene-based piezoresistive sensor. *ACS Nano* **2020**, *14* (2), 2145−2155.

(8) Dong, G.; Yan, L.; Bi, Y. Advanced oxygen evolution reaction catalysts for solar-driven photoelectrochemical water splitting. *Journal of Materials Chemistry A* **2023**, *11* (8), 3888−3903.

(9) Xu, F.; Weng, B. Photocatalytic hydrogen production: an overview of newly advances on structural tuning strategies. *J. Mater. Chem. A* **2023**, *11*, 4473.

(10) Cox, C. R.; Lee, J. Z.; Nocera, D. G.; Buonassisi, T. Ten-percent solar-to-fuel conversion with nonprecious materials. *Proc. Natl. Acad. Sci. U. S. A.* **2014**, *111* (39), 14057−14061.

(11) Novoselov, K. S.; Geim, A. K.; Morozov, S. V.; Jiang, D. -e.; Zhang, Y.; Dubonos, S. V.; Grigorieva, I. V.; Firsov, A. A. Electric field effect in atomically thin carbon films. *science* **2004**, *306* (5696), 666−669.

(12) Dávila, M.; Xian, L.; Cahangirov, S.; Rubio, A.; Le Lay, G. Germanene: a novel two-dimensional germanium allotrope akin to graphene and silicene. *New J. Phys.* **2014**, *16* (9), No. 095002.

(13) Vogt, P.; De Padova, P.; Quaresima, C.; Avila, J.; Frantzeskakis, E.; Asensio, M. C.; Resta, A.; Ealet, B.; Le Lay, G. Silicene: compelling experimental evidence for graphenelike two-dimensional silicon. *Physical review letters* **2012**, *108* (15), No. 155501.

(14) Martínez-Periñán, E.; Down, M. P.; Gibaja, C.; Lorenzo, E.; Zamora, F.; Banks, C. E. Antimonene: a novel 2D nanomaterial for supercapacitor applications. *Adv. Energy Mater.* **2018**, *8* (11), 1702606.

(15) Reis, F.; Li, G.; Dudy, L.; Bauernfeind, M.; Glass, S.; Hanke, W.; Thomale, R.; Schäfer, J.; Claessen, R. Bismuthene on a SiC substrate: A candidate for a high-temperature quantum spin Hall material. *Science* **2017**, *357* (6348), 287−290.

(16) Zhang, L.; Yu, J.; Yang, M.; Xie, Q.; Peng, H.; Liu, Z. Janus graphene from asymmetric two-dimensional chemistry. *Nat. Commun.* **2013**, *4* (1), 1443.
(17) Lu, A. Y.; Zhu, H.; Xiao, J.; Chuu, C. P.; Han, Y.; Chiu, M. H.; Cheng, C. C.; Yang, C. W.; Wei, K. H.; Yang, Y.; Wang, Y.; Sokaras, D.; Nordlund, D.; Yang, P.; Muller, D. A.; Chou, M. Y.; Zhang, X.; Li, L. J. Janus monolayers of transition metal dichalcogenides. *Nat. Nanotechnol.* **2017**, *12* (8), 744−749.
(18) Hajra, D.; Sailus, R.; Blei, M.; Yumigeta, K.; Shen, Y.; Tongay, S. Epitaxial synthesis of highly oriented 2D Janus rashba semiconductor BiTeCl and BiTeBr layers. *ACS Nano* **2020**, *14* (11), 15626−15632. Bianca, G.; Trovatello, C.; Zilli, A.; Zappia, M. I.; Bellani, S.; Curreli, N.; Conticello, I.; Buha, J.; Piccinni, M.; Ghini, M.; Celebrano, M.; Finazzi, M.; Kriegel, I.; Antonatos, N.; Sofer, Z.; Bonaccorso, F. Liquid-Phase Exfoliation of Bismuth Telluride Iodide (BiTeI): Structural and Optical Properties of Single-/Few-Layer Flakes. *ACS Appl. Mater. Interfaces* **2022**, *14* (30), 34963−34974.
(19) Patel, A.; Singh, D.; Sonvane, Y.; Thakor, P.; Ahuja, R. High thermoelectric performance in two-dimensional Janus monolayer material WS-X (X= Se and Te). *ACS Appl. Mater. Interfaces* **2020**, *12* (41), 46212−46219.
(20) Tao, W.-L.; Lan, J.-Q.; Hu, C.-E.; Cheng, Y.; Zhu, J.; Geng, H.-Y. Thermoelectric properties of Janus MXY (M= Pd, Pt; X, Y= S, Se, Te) transition-metal dichalcogenide monolayers from first principles. *J. Appl. Phys.* **2020**, *127* (3), No. 035101.
(21) Chauhan, P.; Singh, J.; Kumar, A. As-based ternary Janus monolayers for efficient thermoelectric and photocatalytic applications. *Journal of Materials Chemistry A* **2023**, *11* (19), 10413−10424.
(22) Liu, M.; Chen, S.-B.; Hu, C.-E.; Cheng, Y.; Geng, H.-Y. Thermoelectric properties of Janus AsSBr monolayer from first-principles study. *Solid State Commun.* **2022**, *342*, No. 114612.
(23) Ali, B.; Idrees, M.; Alrebdi, T. A.; Amin, B.; Alam, Q. Optical and thermoelectric properties of new Janus ZnMN 2 (M= Ge, Sn, Si and N= S, Se, Te) monolayers: a first-principles study. *Nanoscale Advances* **2024**, *6* (2), 680−689.
(24) Gao, P.; Chen, X.; Liu, Z.; Li, J.; Wang, N. Investigation of the lattice thermal transport properties of Janus XClO (X= Cr, Ir) monolayers by first-principles calculations. *Phys. Chem. Chem. Phys.* **2024**, *26* (13), 10136−10143.
(25) Ahmadi, S.; Molla, A. S. S.; Moradi, Z.; Eslami, L. A theoretical prediction of novel Janus NiSX (X= O, Se, Te) Monolayers: Electronic, optical, and thermoelectric properties. *Appl. Surf. Sci.* **2023**, *616*, No. 156560.
(26) Guo, S.-D.; Li, H.-C. Monolayer enhanced thermoelectric properties compared with bulk for BiTeBr. *Comput. Mater. Sci.* **2017**, *139*, 361−367.
(27) Chauhan, P.; Singh, J.; Kumar, A. Mechanical, optical and thermoelectric properties of Janus BiTeCl monolayer. *J. Phys. Chem. Solids* **2022**, *167*, No. 110758.
(28) Sheng, K.; Yuan, H.-K.; Zhang, B. Intrinsic spin, valley and piezoelectric polarizations in room-temperature ferrovalley Janus Ti XY (XY= SCl and SeBr) monolayers. *Nanoscale* **2022**, *14* (40), 15156−15164.
(29) Nandi, P.; Rawat, A.; Ahammed, R.; Jena, N.; De Sarkar, A. Group-IV (A) Janus dichalcogenide monolayers and their interfaces straddle gigantic shear and in-plane piezoelectricity. *Nanoscale* **2021**, *13* (10), 5460−5478.
(30) Guo, S.-D.; Wang, M.-X.; Tao, Y.-L.; Liu, B.-G. Piezoelectric ferromagnetism in Janus monolayer YBrI: a first-principles prediction. *Phys. Chem. Chem. Phys.* **2022**, *25* (1), 796−805.
(31) Cai, X.; Chen, G.; Li, R.; Pan, Z.; Jia, Y. Novel valleytronic and piezoelectric properties coexisting in Janus MoAZ 3 H (A= Si, or Ge; Z= N, P, or As) monolayers. *Journal of Materials Chemistry C* **2024**, *12* (13), 4682−4689.
(32) Varjovi, M. J.; Durgun, E. First-principles study on structural, vibrational, elastic, piezoelectric, and electronic properties of the Janus Bi X Y (X= S, Se, Te and Y= F, Cl, Br, I) monolayers. *Physical Review Materials* **2021**, *5* (10), 104001.
(33) Zhang, W.; Ji, W. Vibrational identification of Janus Pt X O (X= S, Se) monolayers with strong out-of-plane piezoelectricity. *Phys. Rev. B* **2023**, *108* (3), No. 035411.
(34) Gan, W.; Ma, X.; Liao, J.; Xie, T.; Ma, N. First-principles calculation of in-plane and out-of-plane piezoelectric properties of two-dimensional Janus MoSSiX 2 (X= N, P, As) monolayers. *New J. Chem.* **2024**, *48*, 6780.
(35) Bezzerga, D.; Haidar, E.-A.; Stampfl, C.; Mir, A.; Sahnoun, M. Ferro-piezoelectricity in emerging Janus monolayer BMX 2 (M= Ga, In and X= S, Se): ab initio investigations. *Nanoscale Advances* **2023**, *5* (5), 1425−1432.
(36) Yao, M.; Chen, J.; Cai, X.; Tang, Y.; Ni, Y.; Guo, C.; Wang, H.; Sun, B.; Chen, Y. Two-Dimensional Janus Nanostructures M2AB (M= Si, Ge, Sn, A/B= N, P, As) for Piezoelectric Power Generation. *ACS Appl. Nano Mater.* **2024**, *7*, 7773.
(37) Varjovi, M. J.; Ershadrad, S.; Sanyal, B. Structural, vibrational, elastic, electronic, and piezoelectric properties of binary γ− Ge X and ternary γ− Ge 2 X X′ monolayers (X, X′= S, Se, and Te). *Phys. Rev. B* **2023**, *107* (19), No. 195421.
(38) Ju, L.; Bie, M.; Tang, X.; Shang, J.; Kou, L. Janus WSSe monolayer: an excellent photocatalyst for overall water splitting. *ACS Appl. Mater. Interfaces* **2020**, *12* (26), 29335−29343.
(39) Ju, L.; Bie, M.; Shang, J.; Tang, X.; Kou, L. Janus transition metal dichalcogenides: A superior platform for photocatalytic water splitting. *Journal of Physics: Materials* **2020**, *3* (2), No. 022004.
(40) Peng, R.; Ma, Y.; Huang, B.; Dai, Y. Two-dimensional Janus PtSSe for photocatalytic water splitting under the visible or infrared light. *Journal of materials chemistry A* **2019**, *7* (2), 603−610.
(41) Jamdagni, P.; Pandey, R.; Tankeshwar, K. First principles study of Janus WSeTe monolayer and its application in photocatalytic water splitting. *Nanotechnology* **2022**, *33* (2), No. 025703.
(42) Wang, J.; Lu, J.; Zhao, X.; Hu, G.; Yuan, X.; Ren, J. Two-dimensional Janus AsXY (X= Se, Te; Y= Br, I) monolayers for photocatalytic water splitting. *Eur. Phys. J. B* **2023**, *96* (2), 17.
(43) Pan, L.; Zhang, T.; Hu, C.-E.; Chen, X.-R.; Geng, H.-Y. Two-dimensional AlXY (X= S, Se, and Y= Cl, Br, I) monolayers: promising photocatalysts for water splitting with high-anisotropic carrier mobilities. *Journal of Materials Chemistry A* **2022**, *10* (42), 22676−22685.
(44) Kresse, G.; Furthmüller, J. Efficient iterative schemes for ab initio total-energy calculations using a plane-wave basis set. *Phys. Rev. B* **1996**, *54* (16), 11169. Kresse, G.; Joubert, D. From ultrasoft pseudopotentials to the projector augmented-wave method. *Physical review b* **1999**, *59* (3), 1758.
(45) Blöchl, P. E. Projector augmented-wave method. *Phys. Rev. B* **1994**, *50* (24), 17953.
(46) Perdew, J. P.; Burke, K.; Ernzerhof, M. Generalized gradient approximation made simple. *Physical review letters* **1996**, *77* (18), 3865.
(47) Heyd, J.; Scuseria, G. E.; Ernzerhof, M. Hybrid functionals based on a screened Coulomb potential. *J. Chem. Phys.* **2003**, *118* (18), 8207−8215.
(48) Monkhorst, H. J.; Pack, J. D. Special points for Brillouin-zone integrations. *Phys. Rev. B* **1976**, *13* (12), 5188.
(49) Giannozzi, P.; Baroni, S.; Bonini, N.; Calandra, M.; Car, R.; Cavazzoni, C.; Ceresoli, D.; Chiarotti, G. L.; Cococcioni, M.; Dabo, I.; Dal Corso, A.; de Gironcoli, S.; Fabris, S.; Fratesi, G.; Gebauer, R.; Gerstmann, U.; Gougoussis, C.; Kokalj, A.; Lazzeri, M.; Martin-Samos, L.; Marzari, N.; Mauri, F.; Mazzarello, R.; Paolini, S.; Pasquarello, A.; Paulatto, L.; Sbraccia, C.; Scandolo, S.; Sclauzero, G.; Seitsonen, A. P.; Smogunov, A.; Umari, P.; Wentzcovitch, R. M. QUANTUM ESPRESSO: a modular and open-source software project for quantum simulations of materials. *J. Phys.: Condens. Matter* **2009**, *21* (39), No. 395502.
(50) Nosé, S. A unified formulation of the constant temperature molecular dynamics methods. *J. Chem. Phys.* **1984**, *81* (1), 511−519. Hoover, W. G. Canonical dynamics: Equilibrium phase-space distributions. *Phys. Rev. A* **1985**, *31* (3), 1695.

https://doi.org/10.1021/acsomega.4c02874
ACS Omega 2024, 9, 33723−33734

(51) Mandia, A. K.; Muralidharan, B.; Choi, J.-H.; Lee, S.-C.; Bhattacharjee, S. AMMCR: Ab initio model for mobility and conductivity calculation by using Rode Algorithm. *Comput. Phys. Commun.* **2021**, *259*, No. 107697.
(52) Mizokami, K.; Togo, A.; Tanaka, I. Lattice thermal conductivities of two SiO 2 polymorphs by first-principles calculations and the phonon Boltzmann transport equation. *Phys. Rev. B* **2018**, *97* (22), No. 224306.
(53) Zheng, Q.; Chu, W.; Zhao, C.; Zhang, L.; Guo, H.; Wang, Y.; Jiang, X.; Zhao, J. Ab initio nonadiabatic molecular dynamics investigations on the excited carriers in condensed matter systems. *Wiley Interdisc. Rev.: Comput. Mol. Sci.* **2019**, *9* (6), e1411.
(54) Mouhat, F.; Coudert, F.-X. Necessary and sufficient elastic stability conditions in various crystal systems. *Phys. Rev. B* **2014**, *90* (22), No. 224104.
(55) Frantsevich, I. N. Elastic constants and elastic moduli of metals and insulators. In *Reference book* **1982**.
(56) Xiao, W.-Z.; Luo, H.-J.; Xu, L. Elasticity, piezoelectricity, and mobility in two-dimensional BiTeI from a first-principles study. *J. Phys. D: Appl. Phys.* **2020**, *53* (24), 245301. Yang, J. *An introduction to the theory of piezoelectricity*; Springer, 2005.
(57) Arnau, A.; Soares, D. Fundamentals of piezoelectricity. In *Piezoelectric transducers and applications*; Springer Berlin Heidelberg, 2008; pp 1−38.
(58) Tichý, J.; Erhart, J.; Kittinger, E.; Přívratská, J.; Tichý, J.; Erhart, J.; Kittinger, E.; Přívratská, J. Principles of piezoelectricity. *Fundam. Piezoelectr. Sensorics* **2010**, 1−14.
(59) Guo, S.-D.; Guo, X.-S.; Han, R.-Y.; Deng, Y. Predicted Janus SnSSe monolayer: a comprehensive first-principles study. *Phys. Chem. Chem. Phys.* **2019**, *21* (44), 24620−24628.
(60) Yagmurcukardes, M.; Sevik, C.; Peeters, F. Electronic, vibrational, elastic, and piezoelectric properties of monolayer Janus MoSTe phases: A first-principles study. *Phys. Rev. B* **2019**, *100* (4), No. 045415.
(61) Dong, L.; Lou, J.; Shenoy, V. B. Large in-plane and vertical piezoelectricity in Janus transition metal dichalchogenides. *ACS Nano* **2017**, *11* (8), 8242−8248.
(62) Varjovi, M. J.; Yagmurcukardes, M.; Peeters, F. M.; Durgun, E. Janus two-dimensional transition metal dichalcogenide oxides: First-principles investigation of W X O monolayers with X= S, Se, and Te. *Phys. Rev. B* **2021**, *103* (19), No. 195438.
(63) Gan, Y.; Wu, C.-W.; Xie, Z.-X.; Deng, Y.-X.; Zhang, Y.; Zhou, W.-X.; Chen, X.-K. Excellent Medium-Temperature Thermoelectric Performance of Monolayer BiOCl. *Langmuir* **2022**, *38* (25), 7733−7739.
(64) Broido, D.; Ward, A.; Mingo, N. Lattice thermal conductivity of silicon from empirical interatomic potentials. *Phys. Rev. B* **2005**, *72* (1), No. 014308.
(65) Faghaninia, A.; Ager, J. W., III; Lo, C. S. Ab initio electronic transport model with explicit solution to the linearized Boltzmann transport equation. *Phys. Rev. B* **2015**, *91* (23), No. 235123. Miller, N.; Haller, E. E.; Koblmüller, G.; Gallinat, C.; Speck, J. S.; Schaff, W. J.; Hawkridge, M. E.; Yu, K. M.; Ager, J. W., III Effect of charged dislocation scattering on electrical and electrothermal transport in n-type InN. *Phys. Rev. B* **2011**, *84* (7), No. 075315. Ramu, A. T.; Cassels, L. E.; Hackman, N. H.; Lu, H.; Zide, J. M. O.; Bowers, J. E.Rigorous calculation of the Seebeck coefficient and mobility of thermoelectric materials.*J. Appl. Phys.***2010**, *107* (8).083707 Erginsoy, C. Neutral impurity scattering in semiconductors. *Phys. Rev.* **1950**, *79* (6), 1013.
(66) Madsen, G. K.; Singh, D. J. BoltzTraP. A code for calculating band-structure dependent quantities. *Comput. Phys. Commun.* **2006**, *175* (1), 67−71.
(67) Thesberg, M.; Kosina, H.; Neophytou, N. On the Lorenz number of multiband materials. *Phys. Rev. B* **2017**, *95* (12), No. 125206.
(68) Kim, H.-S.; Gibbs, Z. M.; Tang, Y.; Wang, H.; Snyder, G. J. Characterization of Lorenz number with Seebeck coefficient measurement. *APL Mater.* **2015**, *3* (4), No. 041506.
(69) Yang, J.; Xi, L.; Qiu, W.; Wu, L.; Shi, X.; Chen, L.; Yang, J.; Zhang, W.; Uher, C.; Singh, D. J. On the tuning of electrical and thermal transport in thermoelectrics: an integrated theory−experiment perspective. *NPJ Comput. Mater.* **2016**, *2* (1), 1−17.
(70) Rohlfing, M.; Louie, S. G. Electron-hole excitations and optical spectra from first principles. *Phys. Rev. B* **2000**, *62* (8), 4927.
(71) Matthes, L.; Pulci, O.; Bechstedt, F. Massive Dirac quasiparticles in the optical absorbance of graphene, silicene, germanene, and tinene. *J. Phys.: Condens. Matter* **2013**, *25* (39), No. 395305.
(72) Ding, Y.-m.; Nie, X.; Li, Y. Exciton-driven linear and nonlinear optical responses in metal monoxide monolayers M O (M= Mg, Ca, Cd) from first-principles calculations. *Physical Review Materials* **2021**, *5* (7), No. 074005.
(73) Ding, Y. -m.; Ji, Y.; Dong, H.; Rujisamphan, N.; Li, Y. Electronic properties and oxygen reduction reaction catalytic activity of h-ben2 and mgn2 by first-principles calculations. *Nanotechnology* **2019**, *30* (46), 465202.
(74) Komsa, H.-P.; Krasheninnikov, A. V. Effects of confinement and environment on the electronic structure and exciton binding energy of MoS 2 from first principles. *Phys. Rev. B* **2012**, *86* (24), No. 241201.
(75) Chen, S.; Wang, L.-W. Thermodynamic oxidation and reduction potentials of photocatalytic semiconductors in aqueous solution. *Chem. Mater.* **2012**, *24* (18), 3659−3666.
(76) Wang, P.; Liu, H.; Zong, Y.; Wen, H.; Xia, J.-B.; Wu, H.-B. Two-dimensional In2 × 2X′(X and X′= S, Se, and Te) monolayers with an intrinsic electric field for high-performance photocatalytic and piezoelectric applications. *ACS Appl. Mater. Interfaces* **2021**, *13* (29), 34178−34187.
(77) Zafar, Z.; Yi, S.; Li, J.; Li, C.; Zhu, Y.; Zada, A.; Yao, W.; Liu, Z.; Yue, X. Recent development in defects engineered photocatalysts: an overview of the experimental and theoretical strategies. *Energy & Environmental Materials* **2022**, *5* (1), 68−114.
(78) Zhao, X.; Yang, X.; Singh, D.; Panda, P. K.; Luo, W.; Li, Y.; Ahuja, R. Strain-engineered metal-free h-B2O monolayer as a mechanocatalyst for photocatalysis and improved hydrogen evolution reaction. *J. Phys. Chem. C* **2020**, *124* (14), 7884−7892.
(79) Fu, C.-F.; Sun, J.; Luo, Q.; Li, X.; Hu, W.; Yang, J. Intrinsic electric fields in two-dimensional materials boost the solar-to-hydrogen efficiency for photocatalytic water splitting. *Nano Lett.* **2018**, *18* (10), 6312−6317.
(80) Wang, S.; Luo, Q.; Fang, W.-H.; Long, R. Interfacial Engineering Determines Band Alignment and Steers Charge Separation and Recombination at an Inorganic Perovskite Quantum Dot/WS2 Junction: A Time Domain Ab Initio Study. *J. Phys. Chem. Lett.* **2019**, *10* (6), 1234−1241.
(81) Zhang, B.; Li, A.; Lin, J.; Liang, W. Exploring the photocatalytic properties and carrier dynamics of 2D Janus XMMX′(X= S, Se; M= Ga, In; and X′= Te) materials. *Phys. Chem. Chem. Phys.* **2022**, *24* (38), 23437−23446.
(82) Huang, H.; Peng, J.; Li, Z.; Dong, H.; Huang, L.; Wen, M.; Wu, F. Defect-Induced Ultrafast Nonadiabatic Electron−Hole Recombination Process in PtSe2Monolayer. *J. Phys. Chem. Lett.* **2022**, *13* (47), 10988−10993.

https://doi.org/10.1021/acsomega.4c02874
ACS Omega 2024, 9, 33723−33734